Journal of Materials Chemistry C

ROYAL SOCIETY OF CHEMISTRY

PAPER

View Article Online
View Journal | View Issue



Cite this: J. Mater. Chem. C, 2025, 13, 12830

# Spin crossover-driven thermochromic temperature sensor for monitoring heat transfer *via* image analysis†

Bhart Kumar, [a] Kamalesh Tripathy, [b] Mitradip Bhattacharjee [b] and Sanjit Konar *[a]

Received 2nd April 2025,
Accepted 10th May 2025

DOI: 10.1039/d5tc01390a

rsc.li/materials-c

The thermochromic behaviour of spin crossover complexes is desirable for noninvasive thermometry technologies. In this work, we have developed an easy-to-use flexible temperature sensor based on color change accompanying the spin state switching. The sensor consists of an SCO complex, {Fe(Quin)$_2$[Pt(CN)$_4$]} (Quin = quinazoline), embedded in a transparent PDMS substrate using the mould casting method. The decomposition of the colors into individual RGB channels using image analysis provides a straightforward and accurate method for estimating temperature. The qualitative performance trials of the sensor demonstrate its versatility across various applications, including (a) heat transfer monitoring, (b) temperature mapping, and (c) hotspot detection. These trials establish the sensor's ability to operate effectively in a wide range of real-life scenarios.



## Introduction

The recent advancements in diverse fields, such as electronics,[1,2] biomedicine,[3–5] and photonics,[6] have underscored the necessity for versatile, non-invasive thermometry techniques that function effectively regardless of the surface type. The existing thermal imaging methods are based on monitoring the changes in the electromagnetic and optical properties of materials being investigated, such as luminescence,[7,8] reflectivity,[9–11] Raman scattering,[3,12] and electrochromism.[13,14] However, these methods require sophisticated equipment and a complex detection system that involves surface-dependent calibration procedures, making them both expensive and inconvenient to use. Phase change materials (PCMs) that are temperature responsive offer a promising option in terms of thermal sensitivity and readout.[15] In this context, spin crossover materials constitute an important class of PCMs for temperature mapping and surface thermometry applications.[16–18] These are coordination complexes of $d^4$–$d^7$ transition metal ions that can reversibly switch between the low-spin (LS) and high-spin (HS) states under the influence of temperature.[19–23] Various applications of the SCO materials are envisioned depending on the nature of the spin transition. For example, materials with abrupt spin transition ($\Delta T$ = 10 K) facilitate binary temperature detection, attributing to a pronounced change of optical reflectivity.[24] Similarly, complexes exhibiting hysteretic SCO can be used for thermal memory purposes.[25] A very interesting aspect of the spin crossover phenomenon is the significant changes in optical properties (color[26,27] and refractive index[28]) accompanying the switching between the LS and HS electronic configurations. The three channels – red (R), green (G), and blue (B) are the primary components of all colors.[29] Different colors are created by varying the proportions of these channels. There are primary reports establishing a correlation between spin state switching and the associated thermochromism *via* image processing.[30–32] However, no temperature sensor working on SCO-color synergy has been targeted for real-life applications. The existing SCO-based temperature sensors are fabricated either by vacuum deposition, which is only suitable for sublimable complexes, or by compositing with an organic polymer that tends to compromise the spin crossover behaviour.[33–38] The lack of versatility and fabrication effect on the SCO profile are the major bottlenecks associated with existing methods.

In this work, we have designed a flexible temperature sensor that consists of a thermochromic SCO complex, {Fe(Quin)$_2$[Pt(CN)$_4$]}, embedded within a polymeric substrate while preserving its chemical integrity. The color variation associated with the spin transition is correlated with temperature through image processing (Scheme 1). The temperature deduction

[a] Molecular Magnetism Lab, Department of Chemistry, Indian Institute of Science Education and Research Bhopal, Bhopal, MP 462066, India. E-mail: skonar@iiserb.ac.in
[b] i-lab, Electrical Engineering and Computer Science, Indian Institute of Science Education and Research Bhopal, Bhopal, MP 462066, India

† Electronic supplementary information (ESI) available. CCDC 2390485 and 2390486. For ESI and crystallographic data in CIF or other electronic format see DOI: https://doi.org/10.1039/d5tc01390a

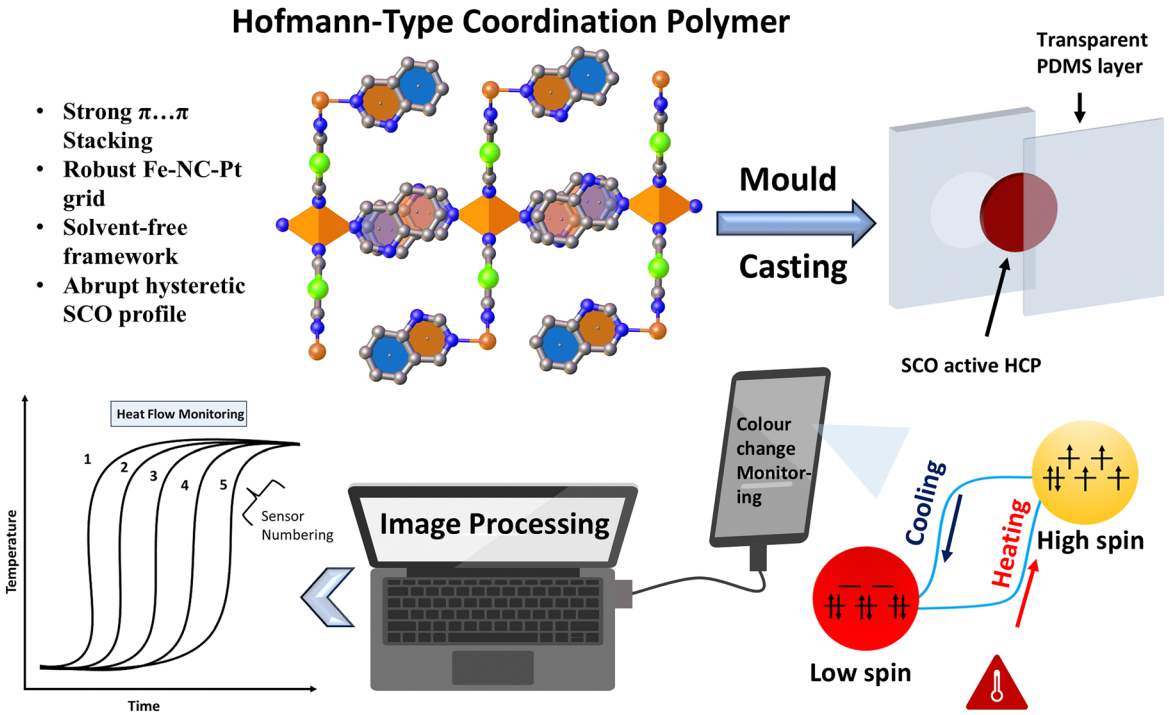


Scheme 1 Illustration of working principle of the SCO-based temperature sensor.

through color channel comparison removes any dependence on the fabrication method or the surface being analyzed, demonstrating the versatility of the method.

The objective of this work is to establish that the developed sensor can effectively monitor heat transfer, by comparing grayscale values with those of a standardized sensor. The method presented achieves temperature monitoring accuracy comparable to that of an infrared thermal camera. Moreover, the sensor can qualitatively map the temperature distribution across a surface.

## Structural details & magnetic behaviour

The single crystal X-ray diffraction analysis at 270 K revealed that the complex crystallizes in a monoclinic crystal system and *C*2/*m* space group. The asymmetric unit consists of one Fe(II) ion, one-fourth of tetracyanoplatinate and a monodentate quinazoline ligand. The Fe(II) ion in the complex has an elongated [$FeN_6$] pseudo-octahedral coordination environment (Fig. 1a). The structure can be described as each Fe(II) ion binding to four cyanide groups of the cyanometallate equatorially, which extends in a 2D fashion, forming bimetallic $\{Fe^{II}[Pt^{II}(CN)_4]\}_n$ layers (ESI,† Fig. S1). The complex exhibits a small deviation of Fe–N–C cyanide angles from 180°, which indicates a strong sigma bond between Fe and N atoms, and hence a stronger ligand field.[39] The ligand quinazoline coordinates axially, connecting the two-dimensional $\{Fe^{II}[Pt^{II}(CN)_4]\}_n$ layers through supramolecular interactions (Fig. 1b).

At 270 K, the complex exhibits a low-spin (LS) state, indicated by the red color of the crystal. When the temperature increases to 325 K, the color changes from red to yellow, signifying a transition to the high-spin (HS) state. The average Fe–N bond length increases from 1.98 Å at 270 K to 2.16 Å at 325 K, which corresponds to a complete spin transition. Similarly, the $FeN_6$ octahedron volume changes from 10.356 $Å^3$ to 13.373 $Å^3$ upon SCO. These changes are communicated throughout the lattice, resulting in a 5.39% increase in unit cell volume. The distortion parameter indicates that the Fe octahedron is less distorted in the HS state ($\Sigma$ = 6.35°) than in the LS state ($\Sigma$ = 8.86°). Slight variations around the Fe(II) centre upon SCO are discernible from the overlay diagram (Fig. 1c). Complex **1** does not undergo a phase change during spin crossover and remains in the monoclinic *C*2/*m* space group, irrespective of the temperature. Details about bond lengths [Å], angles [°], and relevant structural parameters are provided in Table S2 (ESI†).

The bicyclic ligand quinazoline, with its extensive π-electron system, has the potential to facilitate π–π interactions.[40] In adjacent bimetallic $\{Fe^{II}[Pt^{II}(CN)_4]\}_n$ layers, these protruding ligands are packed in an offset face-to-face fashion, resulting in π–π stacking. The supramolecular interactions provide stability to the structure with the centroid-to-centroid distances of 3.706 Å in LS and 3.775 Å in the HS state (ESI,† Fig. S2–S4).

The infrared spectrum of the bulk sample of complex **1** resembled that reported for the analogues of Hofmann-type frameworks.[41] A strong $\nu_{CN}$ stretching vibration band was found at 2173 $cm^{-1}$, whereas in the case of free metallocyanate, the $\nu_{CN}$ peak is observed around 2133 $cm^{-1}$ (ESI,† Fig. S6). To

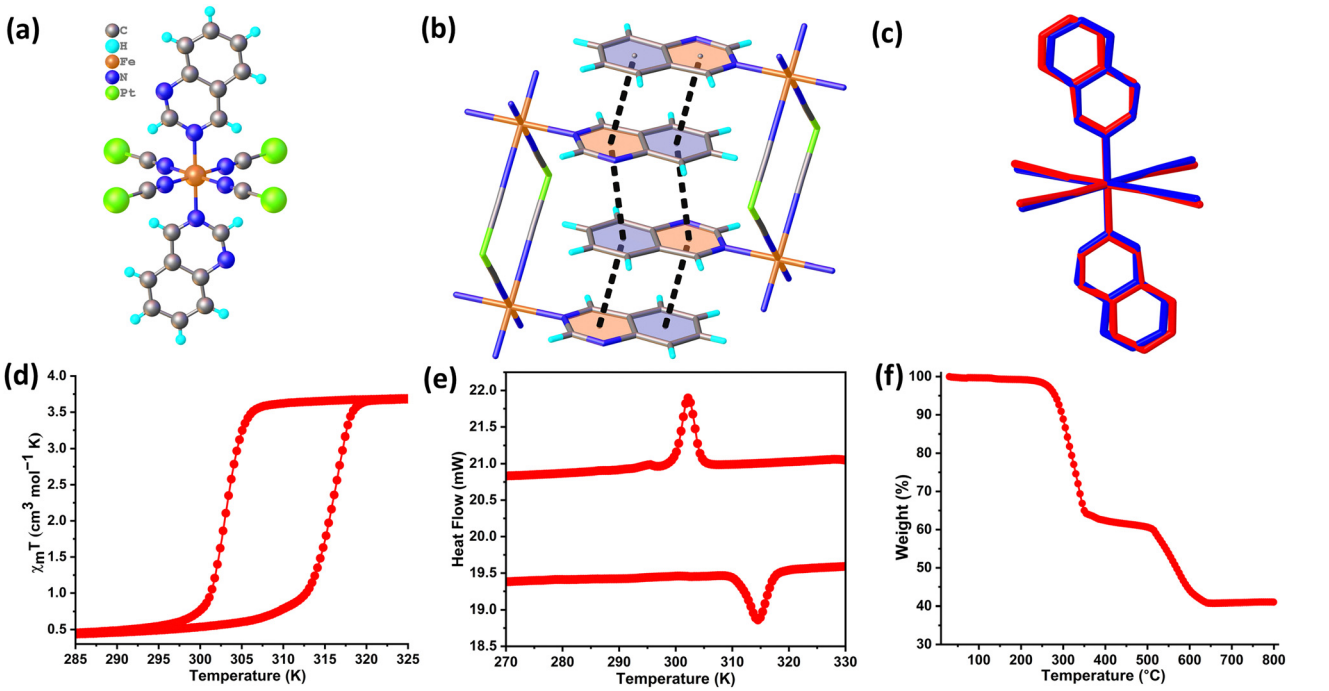


Fig. 1 Crystal structure of complex **1**: (a) fragment representing the $Fe^{II}$ coordination environment, (b) visual representation of the crystal packing demonstrating π···π stacking, (c) overlay diagram (color code: red = high spin and blue = low spin), (d) dc magnetic susceptibility measurement performed on the polycrystalline sample, (e) DSC thermogram of complex **1**, and (f) thermogravimetric analysis of complex **1** confirming the absence of any solvent in the lattice.

verify the phase purity, the PXRD pattern of the bulk sample was compared to the simulated one (ESI,† Fig. S5).

The variable temperature magnetic susceptibility study performed on the bulk crystalline sample revealed an abrupt, single-step hysteretic behaviour (Fig. 1d and Fig. S7, ESI†). At 300 K, the complex is present in the LS state ($\chi_M T$ = 0.45 cm$^3$ K mol$^{-1}$). The spin state switching occurs in a very narrow temperature range of ~7 K. The complex transitions to a complete high-spin state ($\chi_M T$ = 3.65 cm$^3$ K mol$^{-1}$) at 319 K, beginning from a cut-off temperature of 312 K. During the cooling cycle, the complex follows a different path, resulting in hysteresis. The complex remains in the HS state until it reaches the threshold of 307 K and quickly returns to the LS state before it reaches 300 K. The hysteresis width of 13 K is confirmed from the 1st derivative plot (ESI,† Fig. S8). The presence of thermal hysteresis indicates the existence of significant cooperativity.[42,43]

The reproducibility of the SCO behaviour is a major issue for solvent-encapsulating complexes. Therefore, such complexes where the SCO profile does not depend on encapsulated solvents are preferred for application purposes. The absence of solvent in complex **1**, as confirmed by TGA (Fig. 1f), makes the SCO profile easily reproducible. The DSC measurement for complex **1** shows an exothermic peak in cooling mode $T_{1/2}\downarrow$ = 302 K, whereas an endothermic peak centred at $T_{1/2}\uparrow$ = 315 K during the heating cycle (Fig. 1e). Both the phase transition peaks agree quite well with the transition temperatures, as observed in magnetic measurements. Also, the calculated $\Delta H$ (19.137 kJ mol$^{-1}$ and −17.861 kJ mol$^{-1}$) and $\Delta S$ (63.33 J mol$^{-1}$ K$^{-1}$ and −56.77 J mol$^{-1}$ K$^{-1}$) values are consistent with characteristic values reported for Fe(II) SCO complexes.[44–46]

## Sensor design and image processing

To facilitate the practical applications of complex **1**, we have developed a sensor where the complex is sandwiched between transparent PDMS layers without compromising its chemical integrity. The design architecture of the sensor is illustrated in Fig. 2a. It demonstrates a thermochromic behaviour as the spin state changes (Fig. 2b). Notably, the diamagnetic polymer PDMS does not interfere with the spin switching of the complex, as evident from the magnetic measurement of the sensor (ESI,† Fig. S9 and S10).

The thermochromic behaviour of the sensor is attributed to metal-to-ligand charge transfer (MLCT) of complex **1**. The change in the spin state rearranges the electronic configuration of the d-orbitals, which significantly affects the energy and intensity of the MLCT bands.[47,48] In the high-spin state, the elongated metal–ligand bond results in poorer overlap between the metal and ligand orbitals compared to the low-spin (LS) state.[49] The absorption spectrum of complex **1** features a broad MLCT band centred around 510 nm in the low spin state. When the spin state changes to high-spin, this band shifts to 475 nm (see the ESI,† Fig. S13). Consequently, the complex appears red in the low-spin state and changes to yellow in the high-spin

 

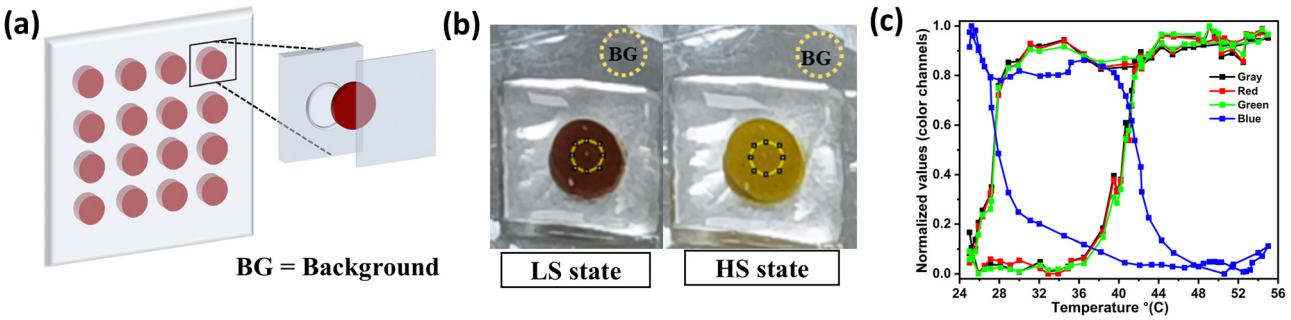


Fig. 2 (a) Schematic depiction of the sensor label showing complex **1** embedded in the polymeric substrate PDMS, (b) actual picture of the sensor label in the LS and HS states, the yellow circle marks the areas under consideration for color decomposition, and (c) the image analysis of the standard sensor depicting color channel evolution with respect to temperature.

state. The reversibility of the sensor has also been evaluated through repeated solid state UV experiments (ESI,† Fig. S13).

The color change accompanying the spin transition has been quantitatively processed into RGB channels using image analysis.[30] To account for the background (BG), the values of the color channels were calibrated using the formula (color channel/BG). The conversion of an image to grayscale simplifies the data by reducing the three color channels to just one, thereby decreasing the processing workload.[50] Also, decomposing the colors into individual channels provides an additional readout of the spin state change, which closely mirrors the $\chi_M T$ *versus* temperature plot of the sensor (as seen in Fig. 2c and Fig. S10, ESI†). This observation confirms that the complex's characteristics remain unchanged during the fabrication process and are effectively integrated into the sensor. Furthermore, the normalized gray channel values (ESI,† Fig. S12) can be viewed as the sensor response, which is useful for various applications.

### Heat transfer monitoring

Extending our investigation towards real-life applications, the sensor was used to monitor heat transfer in a water beaker. The experimental setup included a water beaker placed on a hot plate maintained at 60 °C. Five equidistant sensor labels were affixed to the beaker, as shown in Fig. 3(a). The infrared camera monitored the actual temperature at five height levels, while the color change was observed with a smartphone camera [Fig. 3(a)]. The temperature range under consideration for the heating cycle was a specifically chosen region where the spin states of the complex changed abruptly. To ensure the accuracy of our method, the gray channel values included in the sensor calibration curve were normalized using the formula:

$$\text{Normalized gray values} = \frac{\bar{G} - \bar{G}_{\min}}{\bar{G}_{\max} - \bar{G}_{\min}}, \quad \text{where } \bar{G} = \frac{G}{BG}$$

The temperature values deduced from image processing [Fig. 3(b)] using the sensor calibration curve [Fig. S11, ESI†] were validated against those recorded with the IR camera [Fig. 3(c)]. All sensors provide accurate temperature readings confirmed through a comparison of temperature values from two methods at various times (ESI,† Table S3). Although a small interval of discontinuity was present in the region around sensors 3 and 4. The time domain analysis is an important tool for confirming the direction of heat transfer, as shown in Fig. 3(d). Sensor 1 takes the least time to reach the upper limit of the temperature range under consideration, followed sequentially by sensors 2, 3, 4 and 5. Fig. 3(d) illustrates that the temperature gradient develops from the bottom to the top, thereby confirming that heat transfer occurs in the same direction.

During the cooling process, the water in the beaker was left undisturbed under ambient conditions. The temperature *vs.* time plot revealed a unique cooling pattern [Fig. S14 (ESI†)]. The water at the surface, which is in direct contact with the ambient air, cools faster than the water in the bulk. The molecules at the water–air interface can rapidly release heat to the surrounding air, which kickstarts the fast cooling evident from the temperature profile of sensor 5. For water at lower heights, the cooling pattern is not distinctively clear. The process of heat transfer during cooling is intricate, possibly because it involves the release of heat energy through both convection and conduction.

### Temperature mapping

The sensor was qualitatively tested for temperature mapping applications, and a sensor array consisting of 16 identical circular slots arranged symmetrically was fabricated for this purpose. When the array was exposed to hot air, it underwent a distinct color change from red to yellow indicating conversion of LS to HS, as illustrated in Fig. 4a. Due to the presence of hysteresis in its SCO profile, the color stays yellow even after the removal of the heat source. Furthermore, a doughnut-shaped metal object heated beyond the threshold value was kept in contact with the sensor array, as shown in Fig. 4b. The area of contact facilitated the heat transfer from the metallic body to the sensor label, forming high-temperature zones. The selective thermochromism was also evaluated for the circular disc (ESI,† Fig. S15). The low thermal conductivity of the sensing layer (SCO complex) enables the sensor to show thermochromic change only for the hotspots, rendering it useful for accurate temperature mapping. This feature can aid in monitoring temperature variations and detecting hotspots that exceed the designated threshold.

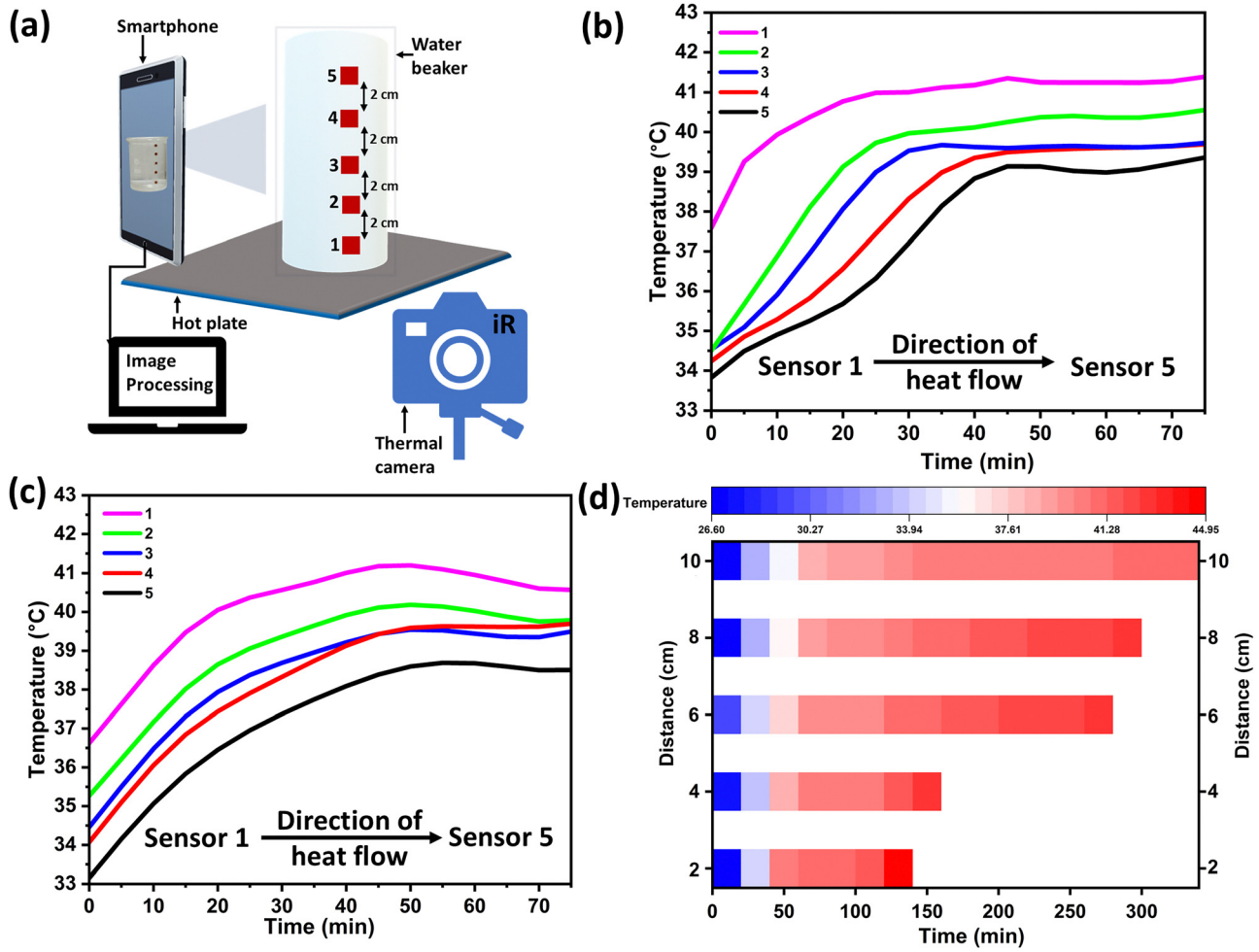


Fig. 3 (a) Schematic representation of the heat transfer monitoring setup, (b) temperature *versus* time profile for the sensors deduced using image processing, (c) temperature *vs.* time profile as monitored through the infrared camera, and (d) time domain analysis.

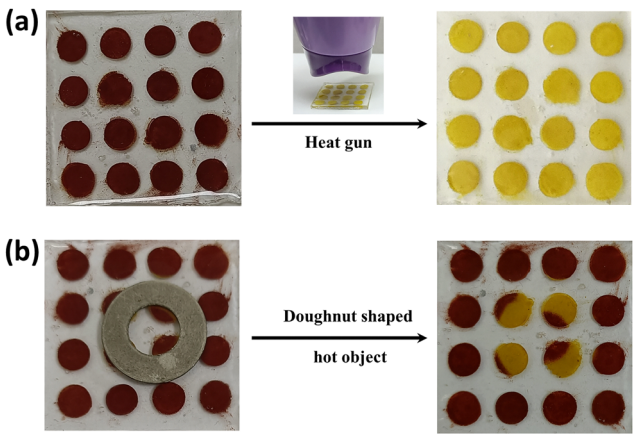


Fig. 4 Temperature distribution monitoring: (a) effect of hot air blow and (b) high-temperature zones generated by a doughnut-shaped object.

## Conclusions

In summary, we have expanded the limited portfolio of hysteretic spin-crossover molecules that operate under ambient conditions. The complex $\{Fe(Quin)_2[Pt(CN)_4]\}$ exhibits switching centred around 310 K (~37 °C) with a hysteresis of 13 K, providing an attractive operational range for various applications.

A flexible polymer-based sensor was developed by embedding the SCO complex in a sandwiched structure. A noteworthy advantage of the fabrication method is that it preserves the molecular integrity of the complex, allowing for the processing of sensitive spin-crossover (SCO) complexes without altering their spin state switching behavior. Additionally, the sensor is conformable to various surface types and has been experimentally proven to be effective for various applications, including heat transfer monitoring, temperature mapping, and hotspot detection.

The operating range of the sensor is limited from 24 °C to 45 °C. Thus, the sensor is suitable for applications only within this temperature range. As the fabrication method is rather a generalised one, different SCO complexes can be used as the active layer to modify the sensor's operating range as required.

We foresee the extension of this work to include different types of complexes with spin state switching across temperature ranges

 

from cryogenic levels to significantly higher ones. Furthermore, a complete standalone system with a user interface can be developed for real-life applications.

## Experimental section

### Synthesis of complex 1

The diffraction quality single crystals of the Hofmann type framework $\{Fe(Quin)_2[Pt(CN)_4]\}$ referred to as complex **1** were obtained by the liquid-to-liquid diffusion method. An aqueous solution (3 mL) of $Fe(ClO_4)_2{\cdot}xH_2O$ (0.03 mmol) is kept at the bottom of the test tube with an ethanolic solution (3 mL) of the tetracyanoplatinate salt (0.03 mmol) and quinazoline ligand (0.06 mmol) at the top, separated by a $H_2O$:EtOH buffer (3 mL). Red-colored crystals were formed around the walls of the test tube after 3–4 weeks. The expected chemical composition of the bulk sample was confirmed by elemental analysis. Calculated composition for $C_{20}H_{12}FeN_8Pt$: C: 39.042%, H: 1.966%, and N: 18.211%. Experimentally found: C: 38.222%, H: 1.931%, and N: 17.93%.

### Sensor fabrication

The sensor includes a transparent PDMS layer fabricated using the mould-casting method with specially designated slots for the SCO complex. Each slot is packed with a uniform dispersion of synthesized SCO material as the sensing layer and is further enclosed by another PDMS layer.

## Data availability

The data supporting this article have been included as part of the ESI.†

## Conflicts of interest

There are no conflicts of interest to declare.

## Acknowledgements

B. K. thanks CSIR, India for the Senior Research Fellowship. K. T. thanks IISER Bhopal for the Senior Research fellowship. S. K. thanks SERB, India (Project no. CRG/2022/001676) for supporting this project. B. K., K. T., M. B. and S. K. thank IISER Bhopal for the instrumentation facilities.

## References

1 M. Mecklenburg, W. A. Hubbard, E. R. White, R. Dhall, S. B. Cronin, S. Aloni and B. C. Regan, *Science*, 2015, **347**, 629–632.
2 Z. Yu, C. Qiu, L. Huang, Y. Gao and D. Tang, *Anal. Chem.*, 2023, **95**, 4212–4219.
3 V. Zani, D. Pedron, R. Pilot and R. Signorini, *Biosensors*, 2021, **11**, 102.
4 J. Shu, Z. Qiu, S. Lv, K. Zhang and D. Tang, *Anal. Chem.*, 2017, **89**, 11135–11142.
5 G. Cai, Z. Yu, P. Tong and D. Tang, *Nanoscale*, 2019, **11**, 15659–15667.
6 L. Jauffred, A. Samadi, H. Klingberg, P. M. Bendix and L. B. Oddershede, *Chem. Rev.*, 2019, **119**, 8087–8130.
7 D. Jaque and F. Vetrone, *Nanoscale*, 2012, **4**, 4301–4326.
8 S. Yakunin, B. M. Benin, Y. Shynkarenko, O. Nazarenko, M. I. Bodnarchuk, D. N. Dirin, C. Hofer, S. Cattaneo and M. V. Kovalenko, *Nat. Mater.*, 2019, **18**, 846–852.
9 G. Tessier, M. Bardoux, C. Boué, C. Filloy and D. Fournier, *Appl. Phys. Lett.*, 2007, **90**, 171112.
10 J. Christofferson, K. Maize, Y. Ezzahri, J. Shabani, X. Wang and A. Shakouri, *J. Electron. Packag.*, 2008, **130**, 041101–041106.
11 J. Christofferson and A. Shakouri, *Rev. Sci. Instrum.*, 2005, **76**, 024903.
12 K. Kumar, O. Stefanczyk, S. Chorazy, K. Nakabayashi and S.-I. Ohkoshi, *Adv. Opt. Mater.*, 2022, **10**, 2201675.
13 P. M. Beaujuge and J. R. Reynolds, *Chem. Rev.*, 2010, **110**, 268–320.
14 C. Gu, A.-B. Jia, Y.-M. Zhang and S. X.-A. Zhang, *Chem. Rev.*, 2022, **122**, 14679–14721.
15 H. Akeiber, P. Nejat, M. Z. A. Majid, M. A. Wahid, F. Jomehzadeh, I. Zeynali Famileh, J. K. Calautit, B. R. Hughes and S. A. Zaki, *Renewable Sustainable Energy Rev.*, 2016, **60**, 1470–1497.
16 G. Li, O. Stefanczyk, K. Kumar, K. Imoto, K. Nakabayashi and S.-I. Ohkoshi, *Chem. Mater.*, 2023, **35**, 9613–9622.
17 L. Salmon, G. Molnár, D. Zitouni, C. Quintero, C. Bergaud, J.-C. Micheau and A. Bousseksou, *J. Mater. Chem.*, 2010, **20**, 5499–5503.
18 K. Senthil Kumar and M. Ruben, *Coord. Chem. Rev.*, 2017, **346**, 176–205.
19 M. A. Halcrow, *Spin-crossover materials: properties and applications*, John Wiley & Sons, 2013.
20 P. Gütlich, A. B. Gaspar and Y. Garcia, *Beilstein J. Org. Chem.*, 2013, **9**, 342–391.
21 B. Kumar, A. Paul, D. J. Mondal, P. Paliwal and S. Konar, *Chem. Rec.*, 2022, **22**, e202200135.
22 A. Bousseksou, G. Molnár, L. Salmon and W. Nicolazzi, *Chem. Soc. Rev.*, 2011, **40**, 3313–3335.
23 O. Kahn and C. J. Martinez, *Science*, 1998, **279**, 44–48.
24 K. Ridier, A.-C. Bas, Y. Zhang, L. Routaboul, L. Salmon, G. Molnár, C. Bergaud and A. Bousseksou, *Nat. Commun.*, 2020, **11**, 3611.
25 O. Kraieva, C. M. Quintero, I. Suleimanov, E. M. Hernandez, D. Lagrange, L. Salmon, W. Nicolazzi, G. Molnár, C. Bergaud and A. Bousseksou, *Small*, 2016, **12**, 6325–6331.
26 F.-J. Valverde-Muñoz, M. Seredyuk, M. C. Muñoz, G. Molnár, Y. S. Bibik and J. A. Real, *Angew. Chem., Int. Ed.*, 2020, **59**, 18632–18638.
27 D. J. Mondal, B. Kumar, A. Paul and S. Konar, *J. Mater. Chem. C*, 2023, **11**, 6750–6759.
28 Y. Zhang, K. Ridier, V. Shalabaeva, I. Séguy, S. Pelloquin, H. Camon, S. Calvez, L. Routaboul, L. Salmon and G. Molnár, *J. Mater. Chem. C*, 2020, **8**, 8007–8011.

29 N. A. Ibraheem, M. M. Hasan, R. Z. Khan and P. K. Mishra, *ARPN J. Sci. Technol.*, 2012, **2**, 265–275.
30 A. Lapresta-Fernández, S. Titos-Padilla, J. M. Herrera, A. Salinas-Castillo, E. Colacio and L. F. C. Vallvey, *Chem. Commun.*, 2013, **49**, 288–290.
31 A. Lapresta-Fernández, M. P. Cuéllar, J. M. Herrera, A. Salinas-Castillo, M. D. C. Pegalajar, S. Titos-Padilla, E. Colacio and L. F. Capitán-Vallvey, *J. Mater. Chem. C*, 2014, **2**, 7292–7303.
32 M. P. Cuéllar, A. Lapresta-Fernández, J. M. Herrera, A. Salinas-Castillo, M. D. C. Pegalajar, S. Titos-Padilla, E. Colacio and L. F. Capitán-Vallvey, *Sens. Actuators, B*, 2015, **208**, 180–187.
33 E. Resines-Urien, M. Á. G. García-Tuñón, M. García-Hernández, J. A. Rodríguez-Velamazán, A. Espinosa and J. S. Costa, *Adv. Sci.*, 2022, **9**, 2202253.
34 Y. Eom, K. Kim, H.-J. Lee, S. R. Torati and C. Kim, *IEEE Magn. Lett.*, 2022, **13**, 1–5.
35 O. Y. Horniichuk, K. Ridier, L. Zhang, Y. Zhang, G. Molnár, L. Salmon and A. Bousseksou, *ACS Appl. Mater. Interfaces*, 2022, **14**, 52140–52148.
36 V. Shalabaeva, S. Rat, M. D. Manrique-Juarez, A.-C. Bas, L. Vendier, L. Salmon, G. Molnár and A. Bousseksou, *J. Mater. Chem. C*, 2017, **5**, 4419–4425.
37 K. S. Kumar and M. Ruben, *Angew. Chem., Int. Ed.*, 2021, **60**, 7502–7521.
38 K. S. Kumar, M. Studniarek, B. Heinrich, J. Arabski, G. Schmerber, M. Bowen, S. Boukari, E. Beaurepaire, J. Dreiser and M. Ruben, *Adv. Mater.*, 2018, **30**, 1705416.
39 W. Liu, L. Wang, Y.-J. Su, Y.-C. Chen, J. Tucek, R. Zboril, Z.-P. Ni and M.-L. Tong, *Inorg. Chem.*, 2015, **54**, 8711–8716.
40 K. Kitase, D. Akahoshi and T. Kitazawa, *Dalton Trans.*, 2024, **53**, 9248–9251.
41 F. J. Valverde-Muñoz, M. Seredyuk, M. C. Muñoz, K. Znovjyak, I. O. Fritsky and J. A. Real, *Inorg. Chem.*, 2016, **55**, 10654–10665.
42 S. Brooker, *Chem. Soc. Rev.*, 2015, **44**, 2880–2892.
43 V. M. Hiiuk, S. Shova, A. Rotaru, V. Ksenofontov, I. O. Fritsky and A. Il'ya, *Chem. Commun.*, 2019, **55**, 3359–3362.
44 M. Ohlrich and B. J. Powell, *J. Chem. Phys.*, 2020, **153**, 104107.
45 L. Piñeiro-López, F. J. Valverde-Muñoz, M. Seredyuk, C. Bartual-Murgui, M. C. Muñoz and J. A. Real, *Eur. J. Inorg. Chem.*, 2018, 289–296.
46 P. Gütlich and H. A. Goodwin, *Spin crossover in transition metal compounds I*, Springer Science & Business Media, 2004.
47 A. Hauser, A. Vef and P. Adler, *J. Chem. Phys.*, 1991, **95**, 8710–8717.
48 T. Delgado, A. Tissot, C. Besnard, L. Guénée, P. Pattison and A. Hauser, *Chem. – Eur. J.*, 2015, **21**, 3664–3670.
49 K. Ridier, A. Hoblos, S. Calvez, M. Lorenc, W. Nicolazzi, S. Cobo, L. Salmon, L. Routaboul, G. Molnár and A. Bousseksou, *Coord. Chem. Rev.*, 2025, **535**, 216628.
50 Z. Yu, H. Gong, M. Li and D. Tang, *Biosens. Bioelectron.*, 2022, **218**, 114751.